Field/valley plasmonic meta-resonances in WS_2-metallic nanoantenna systems: Coherent dynamics for molding plasmon fields and valley polarization

Seyed M. Sadeghi[1,*] and Judy Z. Wu[2]

[1]*Department of Physics and Astronomy, University of Alabama in Huntsville, Huntsville, Alabama 35899, USA*

[2]*Department of Physics and Astronomy, University of Kansas, Lawrence, Kansas 66045, USA*

(Received 28 July 2021; revised 12 January 2022; accepted 13 January 2022; published 24 January 2022)

We theoretically study spin-valley quantum coherence dynamics in a hybrid system consisting of a monolayer of transition metal dichalcogenide (WS_2) and an Ag nanoantenna. For this we map the time evolution of the Bloch and Stokes vectors to investigate, respectively, the dynamics of valley excitons and the states of polarization of plasmon near fields. The results show the formation of two types of collective resonances in the time domain, i.e., valley and field plasmonic meta-resonances (VPMR and FPMR). VPMR is shown as a coherently time-delayed ultrafast rotation of the Block vector. FPMR, on the other hand, occurs as an abrupt change in the near-field polarization of the Ag nanoantenna. The "time of occurrence" (resonance time) of such meta-resonances can be tuned using the intensity and polarization of the laser field responsible for the excitation of the system. Our results show that FPMR can decorate near fields of the Ag nanoantenna at different locations with various types of coherent-field dynamics with nanoscale spatial resolution. VPMR, on the other hand, offers an avenue to control the spin-valley states of transition metal dichalcogenide monolayers using minuscule changes in the intensity and polarization of the incident light.

DOI: 10.1103/PhysRevB.105.035426

I. INTRODUCTION

Recent investigations have shown monolayers (MLs) of transition metal dichalcogenides (TMDs) can offer unique material platforms for the investigation of a broad range of device applications and scientific endeavors. In such materials time reversal symmetry and inversion symmetry breaking impose certain electronic spin orientations (valley index) at specific points at the edge of the Brillouin zone (K and K' valleys). Therefore, in addition to direct band gaps, high absorption coefficients, and very large spin-orbit coupling, they support excitons associated with certain spin-valley configurations of electrons and holes, i.e., K excitons (K-exc) and K' excitons (K'-exc) [1–5]. A key feature of the K and K' valleys is that they support chiral optical selection rules [6]. As a result, they can be addressed individually, providing a unique opportunity for application of spin-valley degrees of freedom of electrons for information processing [4]. These properties, combined with their atomically thin thicknesses, have also made TMD MLs promising candidates for the development of solar cells, photodetectors, light-emitting diodes, phototransistors, and the investigation of coherent processes [1,7–10]. Heterostructures consisting of two crossed deposited TMD MLs, graphene, and single TMD MLs are being utilized for nonvolatile memory cells [11], lasers [9], and large-scale two-dimensional electronics [12]. Hybrid structures consisting of TMD MLs and metallic nanoantennas have also presented a unique area of research for the generation of coherent intervalley dynamics [13–16], Rabi splitting [17–20], the control of polarization and emission of TMD MLs [21,22], the enhancement of second harmonic generation [23], and gain without inversion [24]. Recently, such structures were used to design TMD photodetectors with superior sensitivities [25,26].

TMD MLs provide spin-valley degrees of freedom accessible by right and left circularly polarized (RCP and LCP) light [27,28]. In this paper we utilize such spin-dependent excitations to investigate the formation of valley/field plasmonic meta-resonances (PMRs) in systems consisting of a WS_2 ML and a Ag nanorod [Fig. 1(a)]. PMR was originally introduced in hybrid systems consisting of metallic nanoparticles and semiconductor quantum dots in Ref. [29]. Such a resonance occurs in the time domain when an incident laser beam with a time-dependent amplitude reaches such a hybrid system. PMR is the result of dynamic self-modulation of polarization and field. It appears as a sudden transition in the density of excitons and plasmonic properties of metallic nanoparticles [29,30]. The outcome of these processes is coherently induced time delay in the exciton population and the total field experienced by the quantum dots. PMR has been studied for sensing applications [31–33], fast optical switching processes [34,35], and dynamic rectification [36].

To study valley/field PMRs we consider the interaction of a laser field with a WS_2-metallic nanorod (NR) system, as shown in Fig. 1(a). For the valley PMR (VPMR) the dynamics of spin-valley polarization and exciton population are inspected. By tracing the K valley Bloch vector, we show that VPMR occurs as an upheaval of changes in the exciton concentration and the field experienced by the TMD ML as a function of time. These changes are translated into ultrafast variations in the direction of the Bloch vector. We show that

*seyed.sadeghi@uah.edu

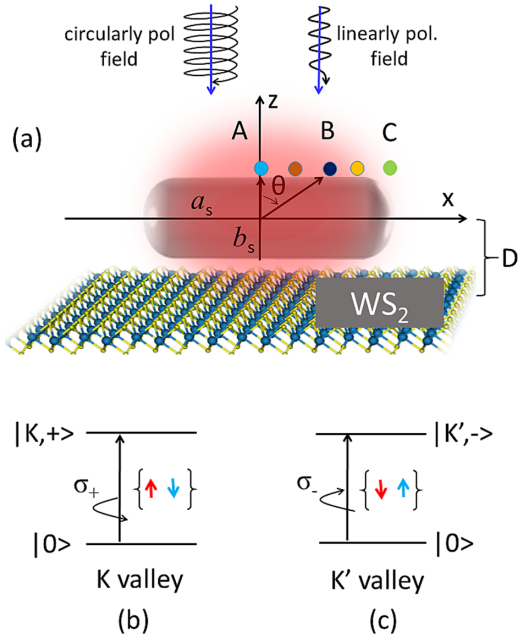

FIG. 1. (a) Schematic illustrations of the WS_2-NR system interacting with either a linearly or circularly polarized laser. Electronic structures of the spin-polarized valley (b) K-exc and (c) K'-exc in the presence of the NR, respectively. The NR has semimajor (a_s) and semiminor (b_s) axes, and it is separated from the WS_2 ML by D.

such processes strongly depend on the polarization of the incident laser field, offering a unique avenue for coherent control of the spin-valley polarization.

Field PMR (FPMR), on the other hand, is a space-time domain resonance of the near-field properties, occurring close to the NR [Fig. 1(a)]. We analyze the ellipticity and Stokes vectors of such a field, demonstrating FPMR not only is spin valley dependent but also strongly depends on the location. Therefore, under the condition that VPMR occurs, for a point right in the middle of the NR [Fig. 1(a), point A] FPMR does not happen. However, as one moves away from the midpoint, the polarization axis of the field starts to rotate as the Stokes parameters are changed from about $100\%Q$ (vertical polarization) to about $100\%U = 1$ (L+45 linear polarization). At a critical location (point B), FPMR happens as an abrupt change in the polarization axis from L+45 to about L−45 ($100\%U = -1$), i.e., 90° counterclockwise rotation.

The outcomes of this paper could be useful for sensor applications wherein one is interested in conformational changes in biological molecules and their chiral properties. The results may also be useful for fast optical and optoelectronic nanoswitches with nanoscale spatial resolution. One expects such devices to be able to convert environmental or optical field variations into coherent spin-valley dynamics with clear signatures in the emission of TMD MLs. Moreover, VPMR and FPMR may offer unique opportunities to control spin-valley polarization using polarization of incident light. Additionally, the system considered in this paper can support the transfer of quantum coherence from one valley (K) to another (K') [37].

II. COHERENT INTERACTION OF VALLEY-POLARIZED EXCITONS WITH PLASMONS

We consider an Ag NR with semimajor and semiminor axes of a_s and b_s placed on the surface of a WS_2 ML with a center-to-center distance of D [Fig. 1(a)]. The material surrounding them is assumed to have dielectric constant ε_0. The WS_2-NR system interacts with a laser field considered to be either RCP or linearly polarized. In the case of the former only the K valley of the WS_2 ML is excited, while for the latter both the K and K' valleys are excited. The way such a system interacts with the RCP laser was already reported [37]. Therefore, in the following we highlight the treatment of the interaction of a linearly polarized light with the WS_2-NR system. For this, note that the electric field of the laser field can be represented by the following:

$$\mathbf{E} = E_0(t)\cos(\omega t)\hat{\mathbf{e}}_\mathbf{x}. \tag{1}$$

Here ω is the frequency of the laser, $E_0(t)$ is its time-dependent amplitude, and $\hat{\mathbf{e}}_\mathbf{x}$ is the polarization unit vector along the x axis [Fig. 1(a)]. We approximate the shape of the NR as a spheroid with polarizability γ given by $\gamma = [\epsilon_m(\omega) - \varepsilon_0]/\{3\varepsilon_0 + 3\kappa[\varepsilon_m(\omega) - \varepsilon_0]\}$. Here κ is the depolarization factor of the spheroid when the incident electric field of the laser is polarized along the x axis. It is given by

$$\kappa = \frac{1-e^2}{e^2}\left[\frac{1}{2e}\ln\left(\frac{1+e}{1-e}\right) - 1\right], \tag{2}$$

where $e = \sqrt{1-1/q^2}$ and $q = a_s/b_s$. Additionally, we describe Ag with the local dynamic dielectric function $\varepsilon_m(\omega) = \varepsilon_{IB}(\omega) + \varepsilon_D(\omega)$, which is a combination of the contribution of d electrons [$\varepsilon_{IB}(\omega)$] and s electrons [$\varepsilon_D(\omega)$] [38].

Considering the optical transition selection rules of the WS_2 ML, the laser field can be decomposed into RCP (σ_+) and LCP (σ_-) components:

$$\mathbf{E} = \frac{1}{\sqrt{2}}E_0(t)\cos(\omega t)(\hat{\mathbf{e}}_+ + \hat{\mathbf{e}}_-), \tag{3}$$

where $\hat{\mathbf{e}}_-$ and $\hat{\mathbf{e}}_+$ refer to the unit vectors in the LCP and RCP bases, respectively. Considering this, under the dipole approximation the interaction Hamiltonian associated with K-exc and K'-exc can have the following form:

$$\hat{H}_{\text{int}} = -\frac{1}{\sqrt{2}}(\mathbf{p}_+ \cdot \mathbf{E}_\mathbf{K} + \mathbf{p}_- \cdot \mathbf{E}_{\mathbf{K}'}). \tag{4}$$

Here $\mathbf{p}_+ = \mu_+\hat{\mathbf{e}}_+$, $\mathbf{p}_- = \mu_-\hat{\mathbf{e}}_-$, $\mathbf{E}_\mathbf{K} = E_K\hat{\mathbf{e}}_+$, and $\mathbf{E}'_\mathbf{K} = E_{K'}\hat{\mathbf{e}}_-$ [39]. μ_+ and μ_- are the dipole moments associated with the σ_+ and σ_- transition components, i.e., K-exc and K'-exc [Figs. 1(b) and 1(c)]. E_K and $E_{K'}$ refer to the fields experienced by K-exc and K'-exc, respectively. They are given as

$$E_K = E^+_{\text{exc}} + E^+_{\text{plas}} + E^{\text{plas}}_{KK} + E^{\text{plas}}_{KK'} + E_{K-K'} \tag{5}$$

and

$$E_{K'} = E^-_{\text{exc}} + E^-_{\text{plas}} + E^{\text{plas}}_{K'K'} + E^{\text{plas}}_{K'K} + E_{K'-K}. \tag{6}$$

In these equations $E^+_{\text{exc}} = E^-_{\text{exc}} = \frac{1}{\sqrt{2}\varepsilon_{\text{eff}}}E_0(t)$, where $\varepsilon_{\text{eff}} = \varepsilon_{\text{ML}}/\varepsilon_0$ and ε_{ML} is the screening dielectric function of the WS_2 ML. These terms represent the external field experienced

by K-exc and K'-exc. The second terms in Eqs. (5) and (6) refer to the field experienced by K-exc and K'-exc via direct excitation of the plasmons by the external field. In regard to these contributions, note that the NR considered here is not chiral and the external field is polarized along the x axis. Considering its frequency and the values of a_s and b_s in this paper, this field can primarily excite only the longitudinal mode of the NR. Having these in mind, we have

$$E^{+}_{\text{plas}} = E^{-}_{\text{plas}} = \frac{S_\alpha P_{\text{NR}}}{\sqrt{2}\varepsilon_{\text{eff}} D^3}. \tag{7}$$

In this equation $P_{\text{NR}} = \gamma a_s b_s^2 E_0(t)$, referring to the polarization of the NR. S_α is polarization factor determined by the direction of the polarization of the laser field with respect to the axis that passes through the NR and is perpendicular to the plane of the WS_2 ML [Fig. 1(a), z axis] [29]. Since this field is polarized along the x axis, we set S_α equal to -1.

The E^{plas}_{KK} and $E^{\text{plas}}_{K'K'}$ terms in Eqs. (5) and (6) refer to the self-induced field of K-exc and K'-exc via interaction with the NR. $E^{\text{plas}}_{KK'}$, on the other hand, represents the field experienced by K-exc via the plasmons excited by K'-exc. $E^{\text{plas}}_{K'K}$ is the field experienced by K'-exc via the plasmons generated by K-exc. The fields generated by K-exc and K'-exc have σ_+ and σ_- polarization states, respectively. Therefore,

$$E^{\text{plas}}_{KK} + E^{\text{plas}}_{KK'} = \frac{S_\alpha^2 \gamma a_s b_s^2}{\varepsilon_{\text{eff}}^2 D^6}(P^{+}_{K} + P^{-}_{K'}), \tag{8}$$

where

$$P^{+}_{K} = \tfrac{1}{2}\mu_+ \rho^{K}_{0,+}, \quad P^{-}_{K'} = \tfrac{1}{2}\mu_- \rho^{K'}_{0,-}. \tag{9}$$

Since the NR is not chiral, the off-diagonal density matrix elements associated with such transitions are equal, i.e., $\rho^{K}_{0,+} = \rho^{K'}_{0,-}$. Assuming $\mu_+ = \mu_-$, we have

$$E^{\text{plas}}_{KK} + E^{\text{plas}}_{KK'} = \frac{S_\alpha^2 \gamma a_s b_s^2}{\varepsilon_{\text{eff}}^2 D^6}\mu_+ \rho^{K}_{0,+}. \tag{10}$$

Similarly, for the case of Eq. (6) we have the following:

$$E^{\text{plas}}_{K'K'} + E^{\text{plas}}_{K'K} = \frac{S_\alpha^2 \gamma a_s b_s^2}{\varepsilon_{\text{eff}}^2 D^6}\mu_- \rho^{K'}_{0,-}. \tag{11}$$

Note that Eqs. (10) and (11) suggest that coherent superposition of the fields of the K and K' excitons generates a linearly polarized field acting on the NR.

The last terms in Eqs. (5) and (6) refer to direct interaction between K-exc and K'-exc. Previous reports have suggested attractive interaction between optically active excitons of opposed spins [40]. Other reports argued that the attractive part of the exciton-exciton interaction, similar to the van der Waals interaction between atoms, is strongly reduced in two-dimensional systems compared to the bulk. Therefore, the short-range repulsive part of the Pauli repulsion dominates [41,42]. In this paper we ignore these terms since we deal with ground state excitons [43].

After applying the rotating wave approximation, Eq. (4) can be written as

$$\hat{H}_{\text{int}} = -\frac{1}{\sqrt{2}}(\mu_+ E_K a^{\dagger}_{+} a_0 + \mu_- E_{K'} b^{\dagger}_{-} b_0) + \text{H.c.} \tag{12}$$

Here $a^{\dagger}_{+}$ ($b^{\dagger}_{-}$) and a_0 (b_0) are the creation and annihilation operators for K-exc (K'-exc) and ground states [Figs. 1(b) and 1(c)]. Introducing $\Omega^{K(K')}_{\text{nor}}$ as the coherently normalized Rabi frequency of K-exc and K'-exc, one can rewrite this equation as

$$\hat{H}_{\text{int}} = \hbar\Omega^{K}_{\text{nor}}(\rho) a^{\dagger}_{+} a_0 + \hbar\Omega^{K'}_{\text{nor}}(\rho) b^{\dagger}_{-} b_0 + \text{H.c.} \tag{13}$$

Here

$$\Omega^{K(K')}_{\text{nor}}(\rho) = \Omega^{K(K')}_{\text{eff}} + \eta\rho^{K(K')}_{0,+(-)}, \tag{14}$$

where $\Omega^{K(K')}_{\text{eff}} = \Omega^{K(K')}_{0}(1 + \frac{S_\alpha \gamma a_s b_s^2}{D^3})$ and $\Omega^{K(K')}_{0} = \frac{\mu_\pm E_0(t)}{2\sqrt{2}\hbar\epsilon_{\text{eff}}}$ refer, respectively, to the Rabi frequency of the WS_2 ML in the presence of pure plasmonic effects (no coherent effects) and in the absence of the NR. We consider the structural parameters of the NR such that its longitudinal plasmon peak happens at a wavelength similar to those of the K-exc and K'-exc. Additionally, $\eta = \frac{S_\alpha^2 \gamma \mu_\pm a_s b_s^2}{\varepsilon_{\text{eff}}^2 D^6}$, and $\frac{1}{\tau_F} = \text{Im}[\eta]$. τ_F refers to the timescale of the Forster resonant energy transfer (FRET) from K-exc and K'-exc to the NR in the absence of quantum coherence. Here since we consider $\mu_- = \mu_+$, the rates for K-exc and K'-exc are the same.

Considering Eqs. (12)–(14), we can find the density matrix that governs the dynamics of excitons in the WS_2-NR system ($\rho^{K,K'}$). Within our assumptions, however, the Hamiltonians for K-exc and K' are independent of each other [Eq. (13)]. Therefore, the density matrices for K-exc (ρ^{K}) and K'-exc ($\rho^{K'}$) are governed by the following:

$$\frac{d\rho^{K(K')}}{dt} = -\frac{i}{\hbar}\big[H_0 + H^{K,(K')}_{\text{int}}, \rho^{K(K')}(t)\big] + [\pounds\rho^{K(K')}]_{\text{damp}}. \tag{15}$$

Here $[\pounds\rho^{K(K')}]_{\text{damp}}$ refers to the damping terms, $H^{K}_{\text{int}} = \hbar\Omega^{K}_{\text{nor}}(\rho) a^{\dagger}_{+} a_0 + \text{H.c.}$ and $H^{K'}_{\text{int}} = \hbar\Omega^{K'}_{\text{nor}}(\rho) b^{\dagger}_{-} b_0 + \text{H.c.}$ H_0 in Eq. (15) refers to the Hamiltonian of the WS_2 in the absence of interaction with the laser field and the NR.

In our treatment for damping $[\pounds\rho^{K(K')}]_{\text{damp}}$, when D is large, we consider the energy (Γ_{ij}) and polarization (γ_{ij}) relaxation rates of K-exc and K'-exc in a phenomenological way [i and $j = 0, +, (-)$] [44,45]. When the WS_2 ML and the NR are close to each other (small D), the polarization dephasing rates associated with K-exc and K'-exc transitions can be influenced by the coherent processes [46]. For the case of K-exc, for example, this leads to

$$\gamma_t = \gamma_{0,+} + \Lambda^{K}_{\text{eff}}, \tag{16}$$

where $\Lambda^{K}_{\text{eff}} = \frac{1}{\tau_F}(\rho^{K}_{0,0} - \rho^{K}_{+,+})$ and $\gamma_{0,+} = \frac{\Gamma_{0,+}}{2} + \gamma_p$ is the depolarization rate of K-exc in the absence of the NR. Here γ_p refers to the pure decoherence rate of K-exc and K'-exc.

Considering these, the density matrix equations for K-exc in the WS_2-NR system have the following form [47,48]:

$$\dot{\rho}^{K}_{0,0} = -2\text{Im}\big[\Omega^{K}_{\text{eff}}\rho^{K}_{+,0}\big] + \Sigma^{K}_{F} + \Gamma_{0,+}\rho^{K}_{+,+}, \tag{17}$$

$$\dot{\rho}^{K}_{+,+} = 2\text{Im}\big[\Omega^{K}_{\text{eff}}\rho^{K}_{+,-}\big] - \Sigma^{K}_{F} - \Gamma_{0,+}\rho^{K}_{+,+}, \tag{18}$$

$$\dot{\rho}^{K}_{+,0} = -\big[i\Delta^{K}_{\text{eff}} + \gamma_t\big]\rho^{K}_{+,0} - i\Omega^{K}_{\text{eff}}\big(\rho^{K}_{0,0} - \rho^{K'}_{+,+}\big). \tag{19}$$

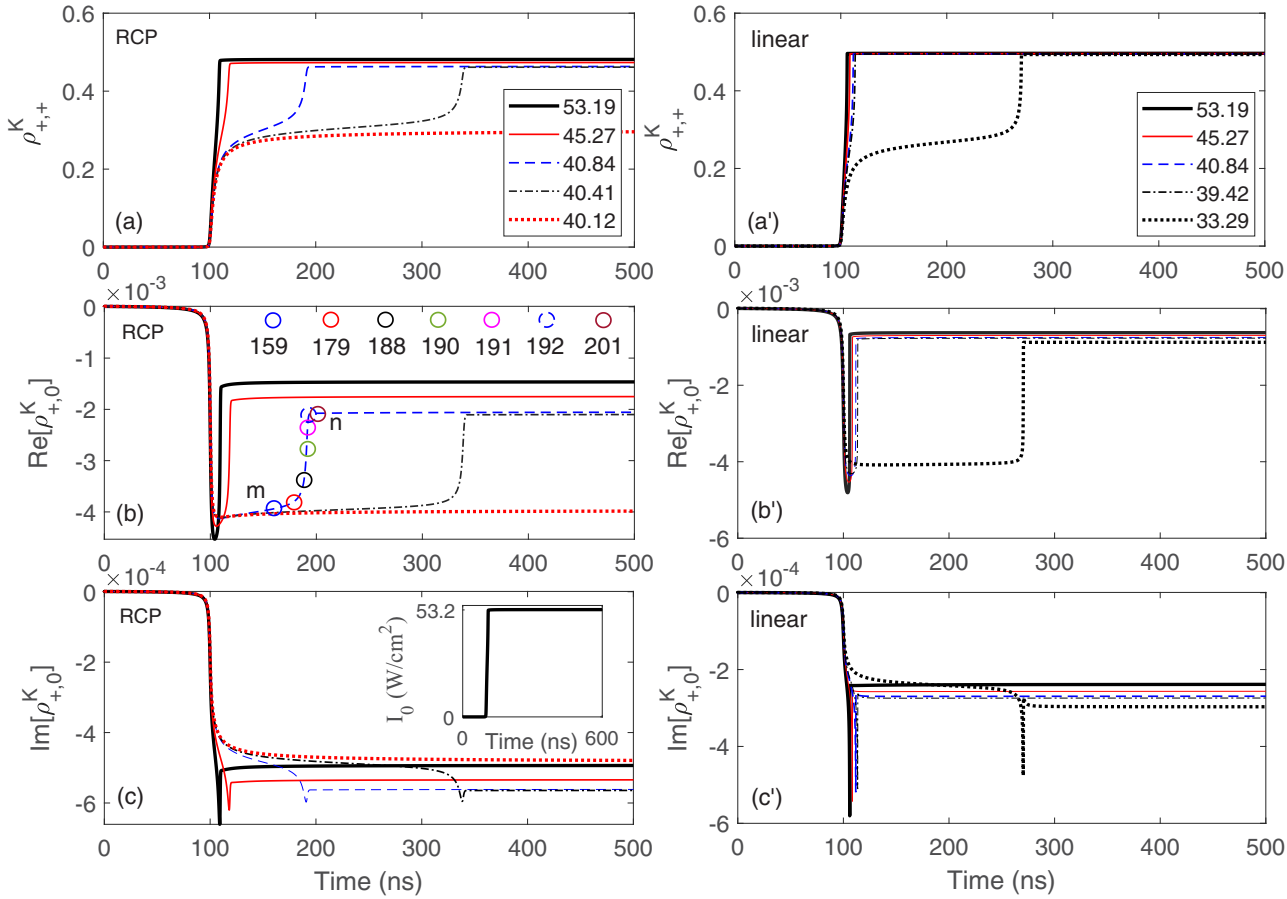

FIG. 2. Variations of (a) $\rho^K_{+,+}$, (b) $\mathrm{Re}[\rho^K_{+,0}]$, and (c) $\mathrm{Im}[\rho^K_{+,0}]$ as a function of time for different values of the laser intensity [legend in (a) is in W/cm^2] when the laser is right circularly polarized. (a′)–(c′) refer to the cases when the laser field is linearly polarized along the x axis. The inset in (c) shows the variation of the intensity of the laser field with time when $I_0 = 53.19$ W/cm^2. The color-coded circles in (b) refer to the sampling times used in Fig. 3. The times associated with these circles are indicated below each circle (in ns).

Here $\Sigma^K_F = 2|\rho^K_{+,0}|^2/\tau_F$, and Δ^K_{eff} is the effective detuning of the K-exc transition from the laser field given by

$$\Delta_{\mathrm{eff}} = \hbar\omega_K - \mathrm{Re}[\eta]\left(\rho^K_{0,0} - \rho^K_{+,+}\right) - \hbar\omega. \tag{20}$$

Here ω_K is the frequency of K-exc, i.e., the $0 \rightarrow |+, K\rangle$ transition [Fig. 1(b)]. Note that Eq. (16) is an important relation, suggesting coherent renormalization of the polarization dephasing rate and the possibility of suppression of quantum decoherence. The latter refers to the case wherein the contribution of the energy transfer Λ^K_{eff} to the overall dephasing process γ_t is reduced as the term $\rho^K_{0,0} - \rho^K_{+,+}$ becomes small.

Note also that the dipole approximation for excitons can be insufficient in cases when the sizes of quantum emitters are comparable with the cavity mode volumes [49–51]. For such cases one may require considering position-dependent exciton-plasmon coupling as the spatial distributions of excitonic and photonic quantum states become important [50]. In the systems considered in this paper, however, the plasmon field modes of the NR have a relatively large volume, and the exciton-plasmon coupling does not fall within the category of the strong-coupling regime. Considering these and the fact that the thickness of the TMD ML is very small, we ignored higher-order multipolar exciton transitions.

III. VALLEY-PLASMONIC META-RESONANCES

Simulations were carried out by solving Eqs. (17)–(19) numerically using ordinary differential equation solvers of MATLAB R2021A. For the initial conditions the values of $\rho^K_{0,0}$ were set to 1, and the rest were zero. To implement this we consider the transition energies of K-exc and K'-exc of WS_2 MLs ($\hbar\omega_K$ and $\hbar\omega_{K'}$) to be 2.006 eV, and the radiative lifetimes Γ_{ij} are about 1.5 ns [19,52]. We also considered μ_- and μ_+ equal to 1.12 $e \times$ nm [19]. In the absence of the NR the linewidths of K-exc ($h\gamma_{0,+}$) and K'-exc ($h\gamma_{0,-}$) were set to 20 meV [52]. Such linewidths, which correspond to the room temperature condition, were reached by setting $\gamma_p = 2.5$ ps^{-1}. Additionally, the thickness of the WS_2 ML is considered to be ∼0.6 nm [20], and its dielectric constant $\varepsilon_{\mathrm{ML}}$ is ∼13.7 [53]. For the Ag NR we assume $a_s = 9$ and $b_s = 4$ nm, and $\varepsilon_0 = 3.61$ (SiN). This leads to a plasmon peak very close to the K and K' valley transitions. The value of D is set to 5.5 nm. The following results are for K-exc. Similar results can also be obtained for K'-exc.

Figure 2 shows the results for variations of $\rho^K_{+,+}$ and $\rho^K_{+,0}$ as a function of time for different values of the laser intensity I_0. The results (thick solid line) show that for RCP and $I_0 = 53.19$ W/cm^2, $\rho^K_{+,+}$ closely follows the field time dependency [Fig. 2(c), inset]. As I_0 becomes smaller, however, the results suggest the formation of a delay in reaching the maximum value of $\rho^K_{+,+}$. This becomes quite evident when $I_0 = 40.84$ W/cm^2 with a delay of about 90 ns (dashed line). For $I_0 = 40.41$ W/cm^2 the delay increases to 237 ns (dash-dotted line), and for $I_0 = 40.12$ W/cm^2 it becomes infinite (dotted line). Figures 2(b) and 2(c) show the corresponding dynamics of the real and imaginary parts of the polarization. In the case of Re$[\rho^K_{+,0}]$, after the delay its absolute the value decreases, while in the case of Im$[\rho^K_{+,0}]$ the opposite occurs. Note that when the distance between the TMD ML and the NR D is very large, one sees only the chiral optical transitions of the TMD ML, including its near-band edge excitonic absorption. Under this condition the NR mostly supports features associated with its localized surface plasmon resonances (LSPRs).

Figures 2(a′)–2(c′) show the corresponding results when the incident laser field is linearly polarized along the x axis. Note that in contrast to the case of RCP, here both the K and K' valleys are excited by the laser field. The results show that for the range of the laser intensity considered for the case of RCP, no significant time delay is generated (thick solid, solid, and dashed lines). In other words, $\rho_{+,+}$ and $\rho_{+,0}$ closely follow the time dependency of the incident laser field. For such a polarization the delay starts to occur at much lower intensity. The dotted lines in Figs. 2(a′)–2(c′) show the results when $I_0 = 33.29$ W/cm^2. Note that the stepwise sharp changes seen in Fig. 2 also depend on the type of TMD materials, as they may have different dipole moments, refractive indices, etc.

The sudden changes in the exciton population of polarization seen in Figs. 2(a)–2(c) refer to VPMR. The physics behind these results can be understood considering the coherent dynamic interplay between exciton band filling, linewidth normalization, and plasmonic-induced line shift. Before the laser reaches the system, the near field of the NR strongly blueshifts the K valley transition and broadens its linewidth via FRET [29,54]. Keeping in mind that the laser field is considered to be resonant with the K-exc, these processes hinder the interaction of the laser with the WS_2-NR system. As the step-rise amplitude of the laser field reaches this system, excitation occurs much more intensely. This causes a reduction of Λ^K_{eff} and Δ^K_{eff} via band filling [Eq. (20)], allowing the laser to become more resonant with the WS_2 transition. This in turn enhances the excitation processes and further suppresses Λ^K_{eff} and Δ^K_{eff}. Such a process leads to a delay in the response of the system to the laser field; that is, VPMR is formed. The results shown in Fig. 2 suggest strong spin-valley dependency of VPMR, as the variation of the incident laser polarization leads to dramatically different results.

To analyze the formation of VPMR further we study the evolution of the Bloch vector associated with the K valley with time. For this, note that the density matrix of the K valley can be written as follows:

$$\rho^K(t) = \begin{pmatrix} \cos^2\left(\frac{\beta(t)}{2}\right) & e^{-i\phi(t)}\cos\left(\frac{\phi(t)}{2}\right)\sin\left(\frac{\beta(t)}{2}\right) \\ e^{i\phi(t)}\cos\left(\frac{\phi(t)}{2}\right)\sin\left(\frac{\beta(t)}{2}\right) & \sin^2\left(\frac{\beta(t)}{2}\right) \end{pmatrix}, \tag{21}$$

where

$$\phi(t) = \tan^{-1}\left(\frac{\text{Im}\left[\rho^K_{+,0}\right]}{\text{Re}\left[\rho^K_{+,0}\right]}\right), \tag{22}$$

$$\beta(t) = \cos^{-1}\left(\rho^K_{0,0} - \rho^K_{+,+}\right). \tag{23}$$

Considering these equations, the unit Bloch vector of the K valley can be given as $\mathbf{r}^K(t) = (u, v, w)$, where

$$u(t) = \cos[\phi(t)]\sin[\beta(t)], \tag{24}$$

$$v = \sin[\phi(t)]\sin[\beta(t)], \tag{25}$$

$$w = \cos[\beta(t)]. \tag{26}$$

Figure 3(a) shows the results for the rotation of the valley Block vector when the incident laser light was right circularly polarized and $I_0 = 40.84$ W/cm^2 [dashed lines in Figs. 2(a)–2(c)]. For this we consider a time period that includes VPMR. As shown in Fig. 2(b) (color-coded circles), this period starts from 159 ns (m) and ends up at 201 ns (n). The numbers below each circle at the top of Fig. 2(b) refers to the sampling time in nanoseconds. Figure 3(b) shows a close-up view of the rotation of the Block vector seen in Fig. 3(a). Here arrow m refers to the state before the transition associated with the VPMR happens (159 ns), and arrow n represents the state after this transition (201 ns).

Note that, as shown in Fig. 3(a), the state of the system before the laser reaches the system is along the w axis (vector G). Therefore, the overall dynamics include a sudden transition from the state characterized by vector G to a state shown by vector n. This is followed by the rotation of vector m to vector n when VPMR occurs. The results in Fig. 3(c) show the case when the incident laser polarization becomes linear while $I_0 = 40.84$ W/cm^2. The results indicate that under the time sampling considered in Fig. 3(b) $\mathbf{r}^K$ undergoes a sudden transition from the ground state (vector G) to state n.

IV. FIELD-PLASMONIC META-RESONANCES

A key aspect of this paper is the prediction of the formation of PMR in the near-field properties of the NR (FPMR). Intuitively, one expects the field around the NR to present dynamics similar to that of the excitons. Our results, however, show this happens only at certain locations. To study FPMR, note that the total electric field at a given point around the NR in the x-z plane [for example, points A, B, and C in Fig. 1(a)] can be written as $\mathbf{E}(r,\theta) = E_z(r,\theta)\hat{\mathbf{e}}_\mathbf{z} + E_x(r,\theta)\hat{\mathbf{e}}_\mathbf{x}$, with $\hat{\mathbf{e}}_\mathbf{z}$ and $\hat{\mathbf{e}}_\mathbf{x}$ referring to the unit vectors along the z and x axes, respectively [Fig. 1(a)]. Each component of this field can be written as $E_i(r,\theta) = E^i_{\text{NR}} + E^i_{\text{app}}$, where $i = x$ and z and E^i_{NR} and E^i_{app} are, respectively, the fields generated by the NR and the applied field at a given location designated by (r,θ). As shown in Fig. 1(a), here r refers to the distance of this location from the center of the NR, and θ is its angle with respect to the z axis. E^z_{NR} and E^x_{NR} can be given as follows:

$$E^z_{\text{NR}}(r,\theta) = -[1 - 3\cos^2(\theta)]E_{\text{NR}}(r), \tag{27}$$

$$E^x_{\text{NR}}(r,\theta) = 3\sin(\theta)\cos(\theta)E_{\text{NR}}(r), \tag{28}$$

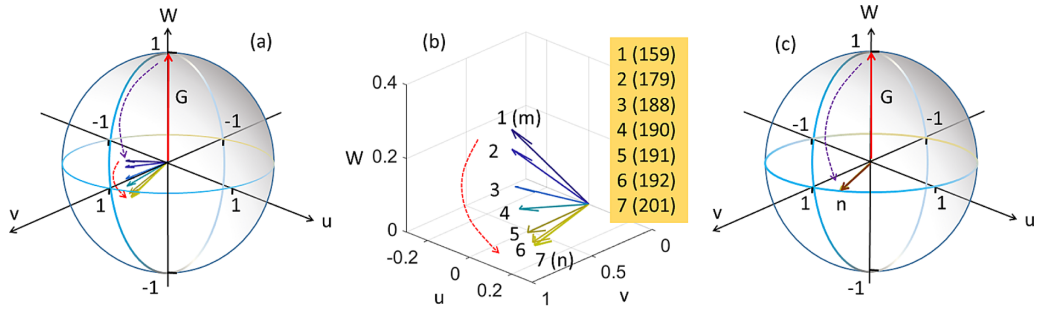

FIG. 3. Variation of $\mathbf{r}^K$ as a function of time in the Bloch sphere when $I_0 = 40.84$ W/cm^2. (a) shows the results when the incident light is right circularly polarized. (b) shows a close-up view of the process seen in (a). (c) presents the results when the incident light is linearly polarized. Other specifications are the same as those in Fig. 2. The curved dashed arrows are used as a guide for the eye of the rotation of Bloch vectors. G in (a) and (c) refer to the state of the system in the absence of the laser. In the legend of (b) the numbers in parantheses show the times associated with each vector (ns).

where $E_{\rm NR}(r) = \frac{\gamma a_s b_s^2}{\varepsilon_o r^3}[E_0 - \frac{\mu_+ \rho^K_{+,0}}{\varepsilon_{\rm eff} D^3}]$. Since we consider the applied field is along the x axis, $E^x_{\rm app} = E_0/2\varepsilon_0$, and $E^z_{\rm app} = 0$.

Note that E_z and E_x can be complex. Additionally, as noted in Ref. [55], for evanescent waves in which fields cannot necessarily be described by two orthogonal field components, one needs to use modified Stokes parameters. In our case, however, because of the symmetry, we consider $S_0 = E_x^* E_x + E_z E_z^*$, $S_1 = E_x E_x^* - E_z E_z^*$, $S_2 = E_x E_z^* + E_z E_x^*$, and $S_3 = i(E_x E_z^* - E_z E_x^*)$. Here S_1/S_0 refers to the dominance of x to z linear polarization, S_2/S_0 refers to that of $+45^\circ$(L+45) to -45° (L$-$45) linear polarization, and S_3/S_0 refers to that of right to left circular polarization. Here L+45 and L$-$45 refer to the linear polarization cases in which the axes of polarization make angles of 45° and -45° with respect to the x axis, respectively.

Figures 4(a)–4(d) show the results for E_z versus E_x (polarization ellipses) under the conditions of Fig. 2 considering $I_0 = 40.84$ W/cm^2 and RCP. For this we scan variations of E_z and E_x over the time period that VPMR occurs [between 159 and 192 nm, as highlighted in Fig. 2(b)]. The scans are carried out in different locations along the x axis. In Fig. 1(a) these positions are shown with solid circles on the top edge of the NR. Each of these locations is indicated with certain values of r and θ. The results show that when $\theta = 0^\circ$ (point A),

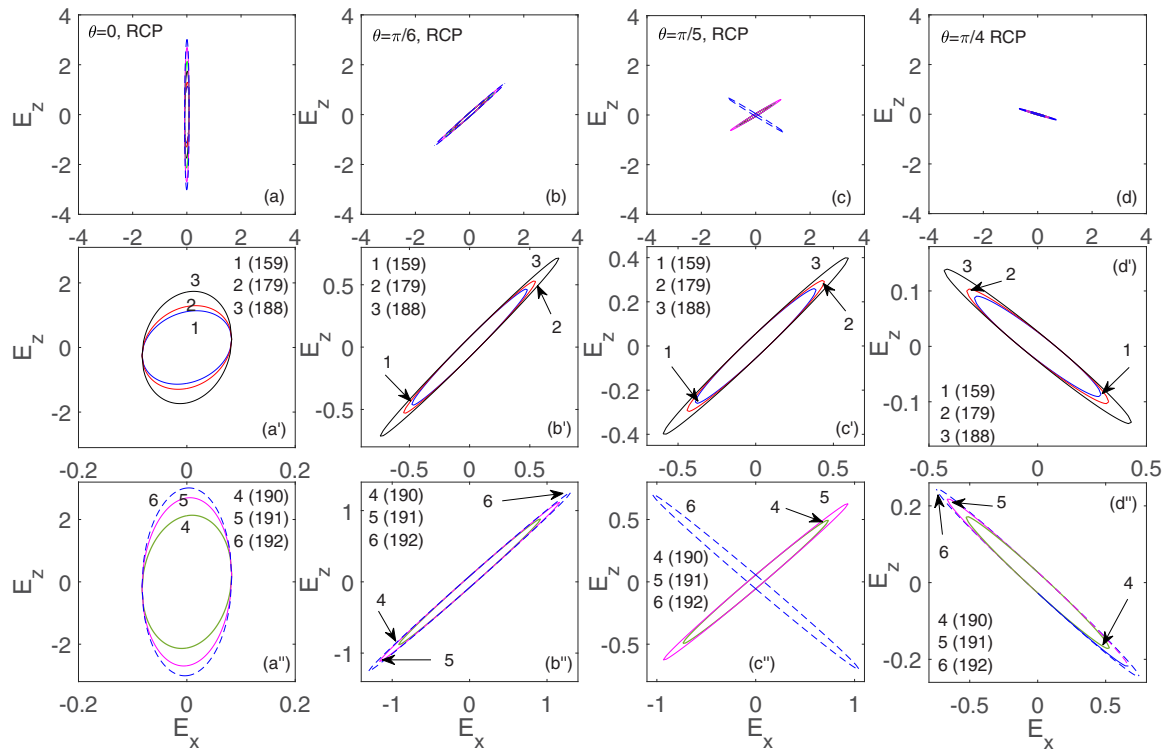

FIG. 4. Dynamics of the polarization ellipses of the NR near field at (a) $\theta = 0^\circ$, (b) $\pi/6$, (c) $\pi/5$, and (d) $\pi/4$. Here (a′)-(a″), (b′)-(b″), (c′)-(c″), and (d′)-(d″) show, respectively, the close-up views of variations of polarization ellipses in (a), (b), and (c). Here $I_0 = 40.84$ W/cm^2, the laser is RCP, and other specifications are the same as those in Fig. 2.

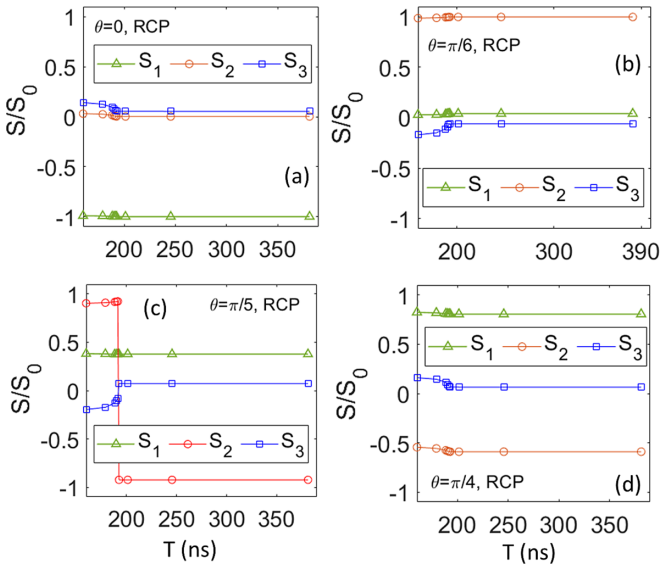

FIG. 5. Variation of S_1 (triangles), S_2 (circles), and S_3 (squares) with time at (a) $\theta = 0^\circ$, (b) $\pi/6$, (c) $\pi/5$, and (d) $\pi/4$. Here $I_0 = 40.84\ \mathrm{W/cm^2}$, the laser is RCP, and other specifications are the same as those in Fig. 2.

the coherently normalized plasmon field remains mostly linearly polarized along the z axis with some small degree of ellipticity [Fig. 4(a)]. The results in Fig. 5(a) confirm this because the normalized Stokes parameters S_2 and S_3 are about zero, while $S_1 \sim -1$. Figures 4(a′) and 4(a″) show the details of the polarization ellipses for this case. Here ellipses 1–6 are associated with sampling times of 159, 179, 188, 190, 191, and 192 ns, respectively.

As seen in Fig. 4(b), for $\theta = \pi/6$ the polarization of the field rotates by about 45°. In Fig. 5(b) this can be seen as the increase of S_2 to about unity (circles), i.e., forming nearly L+45 polarization. Figures 4(b′) and 4(b″) show the details of the evolution of the polarization ellipses shown in Fig. 4(b), indicating no significant changes in the shapes of these ellipses. For $\theta = \pi/5$ [point B in Fig. 1(a)], we note a sudden rotation of the polarization at 192 ns. Figures 4(c′) and 4(c″) show that up to this time, ellipses become mostly larger. At 192 ns, however, a sudden rotation by about −90° happens (ellipse 6). As seen in Fig. 5(c), these results demonstrate the formation of FPMR at this specific position. This process can be seen as the value of S_2 changes from nearly 1 to −1 (circles). For higher values of θ the amplitudes of field start to diminish because within the dipole approximation of the NR, the distance between the center of the NR and the point of interest (point C) increases [Figs. 4(d)–4(d″)]. Figure 4(d) shows that under this condition, the polarization is nearly L−45; that is, the polarization axis is −45° with respect to the x axis. Note that the ellipse associated with 201 ns [point n in Fig. 2(b)] is very similar to that at 192 ns (dashed ellipses); therefore, they are not shown.

To further explore FPMR in Fig. 6 we show the corresponding variations of the Stokes vector as a function of time. Here, similar to the case in Fig. 4, this is done for the range of time in which VPMR occurs, i.e., the time between points m and n indicated in Fig. 2(b). For $\theta = 0^\circ$ the vectors are mostly aligned along one direction [Fig. 6(a)]. In this figure vector m occurs at 159 ns, and vector n occurs at 201 ns. When $\theta = \pi/6$, the results show an overall rotation of these vectors [Fig. 6(b)]. For $\theta = \pi/5$, however, the formation of FPMR can be seen as a sudden rotation of the Stokes vector at 192 ns [Fig. 6(c)]. At 201 ns, indicated by vector m, the system has already undergone the transition. For $\theta = \pi/4$, no significant variation in the Stokes vectors can be seen [Fig. 6(d)]. Note that in Fig. 6, for continuity purposes, we also show Stokes vectors at two more times, i.e., 221 ns (g) and 322 (h).

The results shown in Fig. 4 refer to the case when the incident light was right circularly polarized. If we keep the intensity of the light unchanged, i.e., $40.84\ \mathrm{W/cm^2}$, but consider it to be linearly polarized, the results become quite different. As shown in Fig. 7, under this condition, the near field is more linearly polarized than in the case of RCP when $\theta = 0^\circ$ [Fig. 7(a)]. As θ increases, its ellipticity increases significantly without any significant rotation [Fig. 7(b)]. A further increase of θ forms a linear polarization after a counterclockwise rotation [Figs. 7(c) and 7(d)]. Under this condition, as θ increases, the axis of the polarization undergoes more rotation, while its amplitude decreases. These results can be associated with the phase/amplitude relation of the electronic field components along the x and y axes. The phase difference between these components is influenced by various contributions to the near field at a given location. They include the incident field, the field generated by the plasmons directly generated by the laser field, and the field caused by the dipoles of TMD MLs.

Compared to the cases studied in systems consisting of quantum dots and metallic nanoantennas [29], PMR in TMD-NR systems offers much richer physical processes and applications. This, in particular, is related to the spin-valley configurations of excitons supported by TMD MLs. Selective chiral excitation of the K and K' valleys in such materials

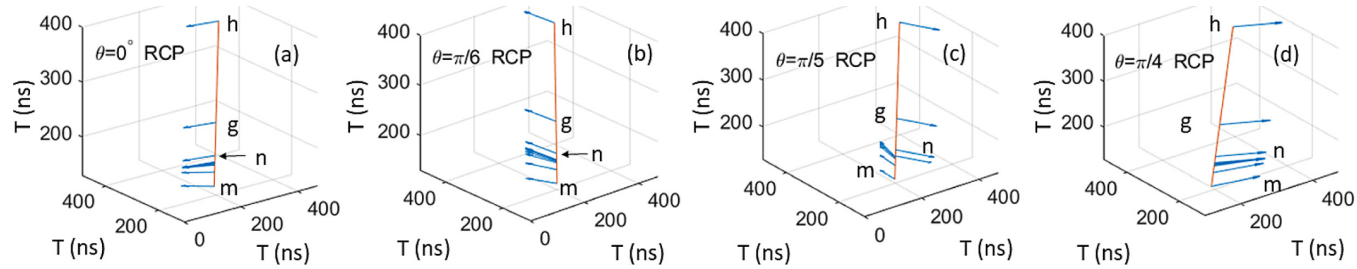

FIG. 6. Variation of the Stokes vector with time for (a) $\theta = 0^\circ$, (b) $\pi/6$, (c) $\pi/5$, and (d) $\pi/5$. All conditions are the same as those in Fig. 4. g and h refer to Stokes vectors at 221 and 322 ns, respectively.

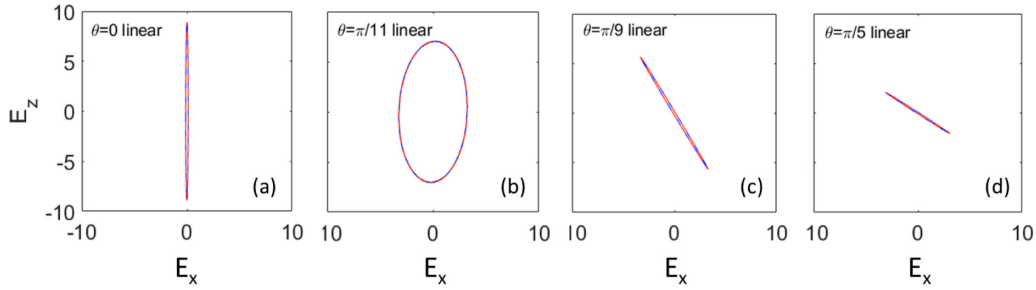

FIG. 7. Dynamics of the polarization ellipse of the NR near field at (a) $\theta = 0^\circ$, (b) $\pi/11$, (c) $\pi/9$, and (d) $\pi/5$ when the incident field is linearly polarized along the x axis. Here $I_0 = 40.84$ W/cm^2, and other specifications are the same as those in Figs. 2(a′)–2(c′).

allows one to generate spin-valley-dependent PMRs which can be controlled uniquely by the polarization of the incident laser field. The plasmonic intervalley coupling in TMD-NR systems allows one to control coherent transfer from one valley to another [37], offering the prospect of coherent switching processes between valleys. On the other hand, the atomically thin monolayer TMD allows stronger exciton-plasmon coupling, which in turn benefits the formation of efficient PMR. Note that the most prominent limiting factor for PMR is the rate of quantum decoherence of K and K' valley polarizations. The impact of this is scaled against the strength of exciton-plasmon coupling. For the structural parameters considered in this paper, when the dephasing time becomes shorter than 400 fs both VPMR and FPMR start to smear out.

V. CONCLUSIONS

We studied plasmonically induced coherent intervalley dynamics generated by the interaction of circularly and linearly polarized laser fields with a hybrid system consisting one ML of WS_2 and an Ag NR. Our results predicted the formation of two types of resonances, called here valley/field plasmonic meta-resonances. VPMR provides coherent control over the spin-valley states of the TMD ML, while FPMR depicts the impact of VPMR in the near field of the NR. Our results showed that FPMR occurs as a sudden variation of the states of polarization of the near field. Spin-valley and field resonances discussed in this paper may have applications in quantum state control of TMD materials, sensors, and light-emitting devices.

ACKNOWLEDGMENTS

This work is supported by the U.S. National Science Foundation (NSF) under Grant No. NSF-ECCS-1917544. J.W. acknowledges support in part by U.S. NSF Contracts No. NSF-DMR-1508494, No. NSF-ECCS-1809293, and No. NSF-DMR-1909292.

[1] K. F. Mak, C. Lee, J. Hone, J. Shan, and T. F. Heinz, Phys. Rev. Lett. **105**, 136805 (2010).
[2] Y. Li, A. Chernikov, X. Zhang, A. Rigosi, H. M. Hill, A. M. van der Zande, D. A. Chenet, E.-M. Shih, J. Hone, and T. F. Heinz, Phys. Rev. B **90**, 205422 (2014).
[3] M. Amani, P. Taheri, R. Addou, G. H. Ahn, D. Kiriya, D.-H. Lien, J. W. Ager III, R. M. Wallace, and A. Javey, Nano Lett. **16**, 2786 (2016).
[4] C. Cong, J. Shang, Y. Wang, and T. Yu, Adv. Opt. Mater. **6**, 1700767 (2018).
[5] G. Moody, J. Schaibley, and X. Xu, J. Opt. Soc. Am. B **33**, C39 (2016).
[6] H. Yu, X. Cui, X. Xu, and W. Yao, Natl. Sci. Rev. **2**, 57 (2015).
[7] W. Bao, X. Cai, D. Kim, K. Sridhara, and M. S. Fuhrer, Appl. Phys. Lett. **102**, 042104 (2013).
[8] C. Tan, Z. Liu, W. Huang, and H. Zhang, Chem. Soc. Rev. **44**, 2615 (2015).
[9] Y. Ye, Z. J. Wong, X. Lu, X. Ni, H. Zhu, X. Chen, Y. Wang, and X. Zhang, Nat. Photon. **9**, 733 (2015).
[10] M. Alamri, M. Gong, B. Cook, R. Goul, and J. Z. Wu, ACS Appl. Mater. Interfaces **11**, 33390 (2019).
[11] S. Bertolazzi, D. Krasnozhon, and A. Kis, ACS Nano **7**, 3246 (2013).
[12] L. Yu, Y.-H. Lee, X. Ling, E. J. Santos, Y. C. Shin, Y. Lin, M. Dubey, E. Kaxiras, J. Kong, H. Wang *et al.*, Nano Lett. **14**, 3055 (2014).
[13] T. Chervy, S. Azzini, E. Lorchat, S. Wang, Y. Gorodetski, J. A. Hutchison, S. Berciaud, T. W. Ebbesen, and C. Genet, ACS Photon. **5**, 1281 (2018).
[14] A. Boulesbaa, V. E. Babicheva, K. Wang, I. I. Kravchenko, M.-W. Lin, M. Mahjouri-Samani, C. B. Jacobs, A. A. Puretzky, K. Xiao, I. Ivanov *et al.*, Acs Photon. **3**, 2389 (2016).
[15] M.-E. Kleemann, R. Chikkaraddy, E. M. Alexeev, D. Kos, C. Carnegie, W. Deacon, A. C. Pury, C. Große, B. Nijs, J. Mertens *et al.*, Nat. Commun. **8**, 1296 (2017).
[16] D. Zheng, S. Zhang, Q. Deng, M. Kang, P. Nordlander, and H. Xu, Nano Lett. **17**, 3809 (2017).
[17] W. Liu, B. Lee, C. H. Naylor, H.-S. Ee, J. Park, A. C. Johnson, and R. Agarwal, Nano Lett. **16**, 1262 (2016).
[18] X. Liu, W. Bao, Q. Li, C. Ropp, Y. Wang, and X. Zhang, Phys. Rev. Lett. **119**, 027403 (2017).
[19] J. Cuadra, D. G. Baranov, M. Wersall, R. Verre, T. J. Antosiewicz, and T. Shegai, Nano Lett. **18**, 1777 (2018).
[20] S. Wang, S. Li, T. Chervy, A. Shalabney, S. Azzini, E. Orgiu, J. A. Hutchison, C. Genet, P. Samorì, and T. W. Ebbesen, Nano Lett. **16**, 4368 (2016).

[21] J. Kern, A. Trugler, I. Niehues, J. Ewering, R. Schmidt, R. Schneider, S. Najmaei, A. George, J. Zhang, J. Lou *et al.*, ACS Photon. **2**, 1260 (2015).
[22] H. Chen, J. Yang, E. Rusak, J. Straubel, R. Guo, Y. W. Myint, J. Pei, M. Decker, I. Staude, C. Rockstuhl *et al.*, Sci. Rep. **6**, 22296 (2016).
[23] X. Han, K. Wang, P. D. Persaud, X. Xing, W. Liu, H. Long, F. Li, B. Wang, M. R. Singh, and P. Lu, ACS Photon. **7**, 562 (2020).
[24] S. M. Sadeghi and J. Z. Wu, Phys. Rev. A **103**, 043713 (2021).
[25] M. Alamri, B. Liu, S. M. Sadeghi, D. Ewing, A. Wilson, J. L. Doolin, C. L. Berrie, and J. Wu, ACS Appl. Nano Mater. **3**, 7858 (2020).
[26] S. A. Ghopry, M. Alamri, R. Goul, B. Cook, S. M. Sadeghi, R. R. Gutha, R. Sakidja, and J. Z. Wu, ACS Appl. Nano Mater. **3**, 2354 (2020).
[27] K. F. Mak, K. He, J. Shan, and T. F. Heinz, Nat. Nanotechnol. **7**, 494 (2012).
[28] H. Zeng, J. Dai, W. Yao, D. Xiao, and X. Cui, Nat. Nanotechnol. **7**, 490 (2012).
[29] S. M. Sadeghi, Phys. Rev. B **79**, 233309 (2009).
[30] S. G. Kosionis and E. Paspalakis, J. Appl. Phys. **124**, 223104 (2018).
[31] S. M. Sadeghi, IEEE Trans. Nanotechnol. **10**, 566 (2010).
[32] S. M. Sadeghi, Appl. Phys. Lett. **101**, 213102 (2012).
[33] A. Hatef, S. M. Sadeghi, É. Boulais, and M. Meunier, Nanotechnology **24**, 015502 (2012).
[34] B. S. Nugroho, A. A. Iskandar, V. A. Malyshev, and J. Knoester, J. Chem. Phys. **139**, 014303 (2013).
[35] H. Hapuarachchi, S. D. Gunapala, and M. Premaratne, J. Phys.: Condens. Matter **31**, 325301 (2019).
[36] F. Carreño, M. A. Antón, and E. Paspalakis, J. Appl. Phys. **124**, 113107 (2018).
[37] S. M. Sadeghi and J. Z. Wu, ACS Photon. **6**, 2441 (2019).
[38] A. Hatef, S. M. Sadeghi, S. Fortin-Deschênes, E. Boulais, and M. Meunier, Opt. Express **21**, 5643 (2013).
[39] M. Tokman, Y. Wang, and A. Belyanin, Phys. Rev. B **92**, 075409 (2015).
[40] C. Robert, D. Lagarde, F. Cadiz, G. Wang, B. Lassagne, T. Amand, A. Balocchi, P. Renucci, S. Tongay, B. Urbaszek, and X. Marie, Phys. Rev. B **93**, 205423 (2016).
[41] S. Schmitt-Rink, D. S. Chemla, and D. A. B. Miller, Phys. Rev. B **32**, 6601 (1985).
[42] P. Le Jeune, X. Marie, T. Amand, F. Romstad, F. Perez, J. Barrau, and M. Brousseau, Phys. Rev. B **58**, 4853 (1998).
[43] V. Shahnazaryan, I. Iorsh, I. A. Shelykh, and O. Kyriienko, Phys. Rev. B **96**, 115409 (2017).
[44] P. R. Eastham, A. O. Spracklen, and J. Keeling, Phys. Rev. B **87**, 195306 (2013).
[45] J. del Pino, J. Feist, and F. J. Garcia-Vidal, New J. Phys. **17**, 053040 (2015).
[46] S. M. Sadeghi and K. D. Patty, Appl. Phys. Lett. **104**, 083101 (2014).
[47] S. M. Sadeghi, A. Hatef, and M. Meunier, Appl. Phys. Lett. **102**, 203113 (2013).
[48] S. M. Sadeghi, W. J. Wing, and R. R. Gutha, Nanotechnology **26**, 085202 (2015).
[49] A. Cuartero-González and A. I. Fernández-Domínguez, Phys. Rev. B **101**, 035403 (2020).
[50] T. Neuman, R. Esteban, D. Casanova, F. J. García-Vidal, and J. Aizpurua, Nano Lett. **18**, 2358 (2018).
[51] M. K. Svendsen, Y. Kurman, P. Schmidt, F. Koppens, I. Kaminer, and K. S. Thygesen, Nat. Commun. **12**, 2778 (2021).
[52] K. M. McCreary, M. Currie, A. T. Hanbicki, H.-J. Chuang, and B. T. Jonker, ACS Nano **11**, 7988 (2017).
[53] A. Laturia, M. L. Van de Put, and W. G. Vandenberghe, npj 2D Mater. Appl. **2**, 6 (2018).
[54] W. Zhang, A. O. Govorov, and G. W. Bryant, Phys. Rev. Lett. **97**, 146804 (2006).
[55] T. Setälä, A. Shevchenko, M. Kaivola, and A. T. Friberg, Phys. Rev. E **66**, 016615 (2002).